Resistance of full-scale beams against close-in explosions. numerical modeling and field tests

Resistance of full-scale beams against close-in explosions. numerical modeling and field tests

A. Prado, A. Alañon, R. Castedo, A.P. Santos, L.M. López, M. Chiquito, M. Bermejo, C. Oggeri

PII: S2214-9147(24)00109-0

DOI: https://doi.org/10.1016/j.dt.2024.05.002

Reference: DT 1439

To appear in: *Defence Technology*

Received Date: 16 December 2023

Revised Date: 13 March 2024

Accepted Date: 8 May 2024

Please cite this article as: Prado A, Alañon A, Castedo R, Santos AP, López LM, Chiquito M, Bermejo M, Oggeri C, Resistance of full-scale beams against close-in explosions. numerical modeling and field tests, *Defence Technology*, https://doi.org/10.1016/j.dt.2024.05.002.

Resistance of full-scale beams against close-in explosions. numerical modeling and field tests

A. Prado[a], A. Alañon[a], R. Castedo[b,*], A.P. Santos[b], L.M. López[b], M. Chiquito[b], M. Bermejo[c], C. Oggeri[d]

[a]Escuela Politécnica Superior de Ávila, Universidad de Salamanca, 05003 Ávila, Spain

[b]E.T.S.I. Minas y Energía, Universidad Politécnica de Madrid, 28003 Madrid, Spain

[c]Department of Engineering, Aviation and Technology, Saint Louis University, 28003 Madrid, Spain

[d]Department of Environment, Land and Infrastructure Engineering (DIATI), Politecnico di Torino, 10129 Torino, Italy

**Corresponding author:* ricardo.castedo@upm.es

Resistance of full-scale beams against close-in explosions. numerical modeling and field tests

Abstract

This paper explores the performances of a finite element simulation including four concrete models applied to a full-scale reinforced concrete beam subjected to blast loading. Field test data has been used to compare model results for each case. The numerical modelling has been, carried out using the suitable code LS-DYNA. This code integrates blast load routine (CONWEP) for the explosive description and four different material models for the concrete including: Karagozian & Case Concrete, Winfrith, Continuous Surface Cap Model and Riedel–Hiermaier–Thoma models, with concrete meshing based on 10, 15 and 20 mm. Six full-scale beams were tested: four of them used for the initial calibration of the numerical model and two more tests at lower scaled distances. For calibration, field data obtained employing pressure and accelerometers transducers were compared with the results derived from the numerical simulation. Damage surfaces and the shape of rupture in the beams have been used as references for comparison. Influence of the meshing on accelerations has been put in evidence and for some models the shape and size of the damage in the beams produced maximum differences around 15%. In all cases, the variations between material and mesh models are shown and discussed.

Keywords: Blast test; Numerical simulation; LS-DYNA; Concrete model; Mesh effect; Full-scale beams.

1. Introduction

Today, the increase in terrorist activities and concerns about accidental explosions have led to a great deal of attention being paid to the blast resistance capacity of buildings and various types of constructive elements like slabs, beams, columns, etc. Reinforced concrete (RC) is one of the main construction materials for multiple reasons, such as its price, weather and fire resistance, formability, and favorable mechanical properties. The importance of understanding and studying the response of concrete structures (or elements) to explosive loads continues to grow, as it increases the safety of the structure as well as the people in it. Due to the high economic costs associated with these types of tests, especially full-scale ones, and the challenges in handling and monitoring them, blast resistance tests are usually conducted on smaller scales. However, this can sometimes lead to incorrect conclusions when extrapolated to full-scale specimens [1], so assumptions drawn in such cases should be extrapolated with some caution [2]. For all these reasons, it is possible to imagine that nowadays the number of papers in open sources on full-scale complete structures is scarce. Among the literature

found, it can be highlighted the work of Bermejo et al. [3] with the sudden withdrawal of a pillar on a two-span, two-high RC structure; Xiao et al. [4] investigate the effects of external explosions to a two-story masonry and RC building with a gable roof by means of full-scale experiments and numerical simulations; or the work of Santos et al. [5] where numerous improvised explosive devices (IEDs) were tested inside a RC structure. However, there are more publications on structural elements, especially on RC slabs tests accompanied by numerical models [6,7], and, to a lesser extent, work on columns or beams that also incorporate tests and modeling [8,9]. Finally, it is worth mentioning recent publications as a review of the state of the art, such as the work of Lukic & Draganic [10] on columns, that of Anas et al. [11] on slabs, that of Zhang et al. [12] on different structural elements or that of Alshaikh et al. [13] on the progressive collapse of complete structures.

Due to the above reasons, more and more research tends to rely on numerical modeling. Numerical modeling is a good alternative and a very useful tool, but in the case of blast loading, it must be calibrated and validated by appropriate field tests. There are several programs that can be used for the simulation of nonlinear dynamic responses in structural contexts, i.e. AUTODYN [14], LS-DYNA [15]. LS-DYNA offers a wide range of concrete constitutive models (more than fifteen), including Karagozian & Case Concrete (KCC) Model (Mat_Concrete_Damage_Rel3 or MAT072R3), Winfrith model (Mat_Winfrith_Concrete or MAT084), Continuous Surface Cap Model or CSCM Model (Mat_CSCM_Concrete or MAT159), and Riedel–Hiermaier–Thoma or RHT model (Mat_RHT or MAT272). For example, Su et al. [16] calibrate the KCC model for use with ultra-high-performance concrete (UHPC) based on an extensive literature review. The authors then compare the results of the self-generated and the calibrated model against impact and blast tests; in both cases the outcomes are quite good. Shi et al. [17] present a paper on the protection of RC columns, defined with the KCC model, against near or intermediate blast (scaled distance between 0.52 and 0.69 $m \cdot kg^{-1/3}$) with granite slab protection. The results show an acceptable performance of the model with respect to the size of the damage produced. Thai et al. [18] propose an empirical equation for the residual strength of RC columns with fibers against blast, all performed by a numerical study with the Winfrith model. Using the same material model, López et al. [19] present a numerical model of a full-scale two-span structure validated against the detonation of three explosive charges at different locations and positions of the structure. Lee & Kwak [20] develop an orthotropic model for concrete and validate it against the CSCM and the KCC model based on full-scale slabs tests against blasting published by Castedo et al. [21]. Liu et al. [22] also employs the CSCM model but this time for the calibration of a geopolymer-based ultrahigh- performance concrete (G-UHPC) in slabs subjected to contact explosions. Wu et al. [23] and Zhao et al. [24] employ the RHT model to reproduce the behavior of RC slabs and beams against near blast, respectively. A common feature of the highlighted models is their ease of use by directly entering a minimum number of concrete input data, thereby automatically generating the rest

of the parameters. However, to realistically predict the performances of RC structures or elements under different loads, the constitutive model should capture the most basic behaviors of concrete. The use of one model or another can significantly affect the simulation result, so knowing their advantages and disadvantages, their behaviors in comparison with different parameters measured in tests (i.e. accelerations, damage areas), along with as a function of mesh size is crucial to avoid unrealistic results. Nonetheless, there is not much literature that, for the same case with real tests, presents a comparison of the numerical results as a function of the model used [25–27].

In addition, LS-DYNA offers a spectrum of different techniques for the description of the blast load and its interaction with the structures subjected to it. The first technique is an empirical method that applies pressure-time curves (ConWep approach including in LS-DYNA by the Load Blast Enhanced (LBE) module [28,29]), it is a fast and reliable calculation method but applicable in cases where reflections are not critical. The second, Multi-Material Arbitrary Lagrangian-Eulerian (MM-ALE) [18,30], is a method based on the expansion of the explosive by the surrounding medium (generally air) that requires significant computational resources, in addition to knowledge of the equation of state of the explosive to be used. The third is a mixed method between the first two, to reduce calculation times, where the pressure-time curves are applied to a volume of air, and from there the air wave is transmitted (commonly known as LBE-ALE [31,32]). The last two techniques (Smooth Particle Hydrodynamic [33,34]; and Particle Blast Method [35]) are meshless methods, which are highly dependent on the number of elements, with a high computational cost, and where it is almost impossible to know the pressure applied by the explosive to the structural element. In addition to its characteristics, also the mass and the distance of the explosive to the target determine the use of one technique or another [1,36].

For the purposes of this investigation, a 3D full-scale Lagrangian finite element (FE) model has been created using the LS-DYNA software, specifically Version 971–R12, and compared with field test. The primary aim is to enhance comprehension and insight into the effects of close-range explosions on concrete structures, focused on RC beams. To encompass the diversity inherent in concrete, four distinct material models have been applied also analyzing their mesh sensitivity. In the context of the FE model, the explosive charge is simulated using the LBE technique. The outcomes produced by these models have been compared to the results obtained from full-scale field tests.

2. Test description and instrumentation

In 2011, within the framework of the “SEGTRANS” project funded by the Center for the Development of Industrial Technology (CDTI, Government of Spain), tests were carried out at the Technological Institute of “La Marañosa” on different full-scale structural elements: slabs [21] and beams, all of them built with reinforced concrete. The tests, based on the scaled distance (Z), can be

classified as average field for the cases B1, B2, B3 and B4, upper near-field limit for the test B5 and near field for test B6, following the classification adapted from Hilding [36] and Castedo et al. [21]. The test set-up is shown in Table 1.

Table 1

Tests characteristics. Regarding the instrumentation used in the tests: "P" refers to air blast pressure sensors; "a" to accelerometers located on the slabs; "HSV" to high-speed video; and "SM" to Schmidt hammer.

Test #	Charge setup			Instrumentation
	Standoff distance/ m	Equivalent TNT mass (W)/kg	Scaled distance (Z)/ ($m \cdot kg^{-1/3}$)	
B1	1	2	0.8	P+a+HSV+SM
B2	1	2	0.8	P+a+HSV+SM
B3	1	2	0.8	P+a+HSV+SM
B4	1	4	0.63	P+a+HSV+SM
B5	1	15	0.4	HSV+SM
B6	0.5	15	0.2	HSV+SM

For the testing, PG2, a plastic explosive with similarities to C4 and comprising 86% RDX, was used. This explosive was chosen because it is chemically safe, readily moldable and has a well-characterized TNT equivalent on a pressure basis of 1.4 [37]. Three different charges were used, with spherical shape for the low ones (2 and 4 kg of TNT Equivalent); and according to the charge shape classification of the UFC [38] the high charge (15 kg of TNT Equivalent) can be considered an intermediate case between cylindrical, in-process hopper (cube) or bag (see Fig. 1). Note that the foam cube used for test B5 is just acting as a placeholder and the possibility of a shockwave reflection on the foam can be rejected. In all cases, the charge was initiated in the center with a conventional detonator inserted from the top of the load. The charges were also centered above each beam, as can be seen in Figs. 1 and 2.

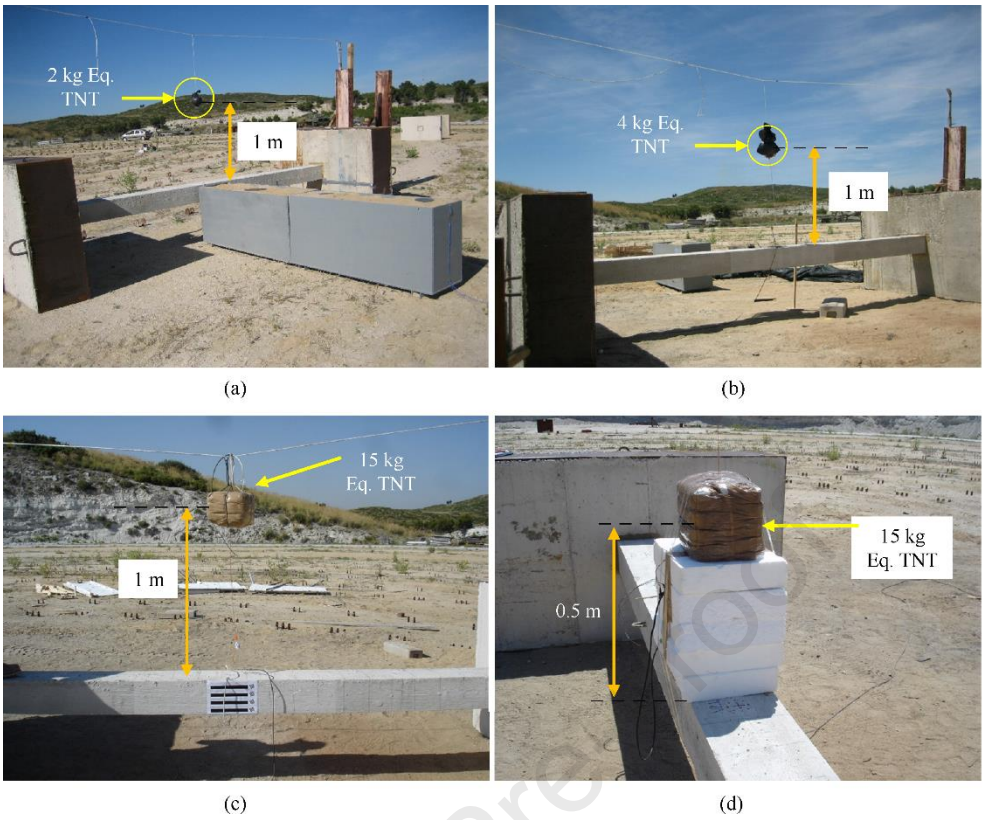

Fig. 1. Images of the experimental field campaign: (a) Beam B1 (same settings as B2 and B3); (b) Beam B4; (c) Beam B5; (d) Beam B6.

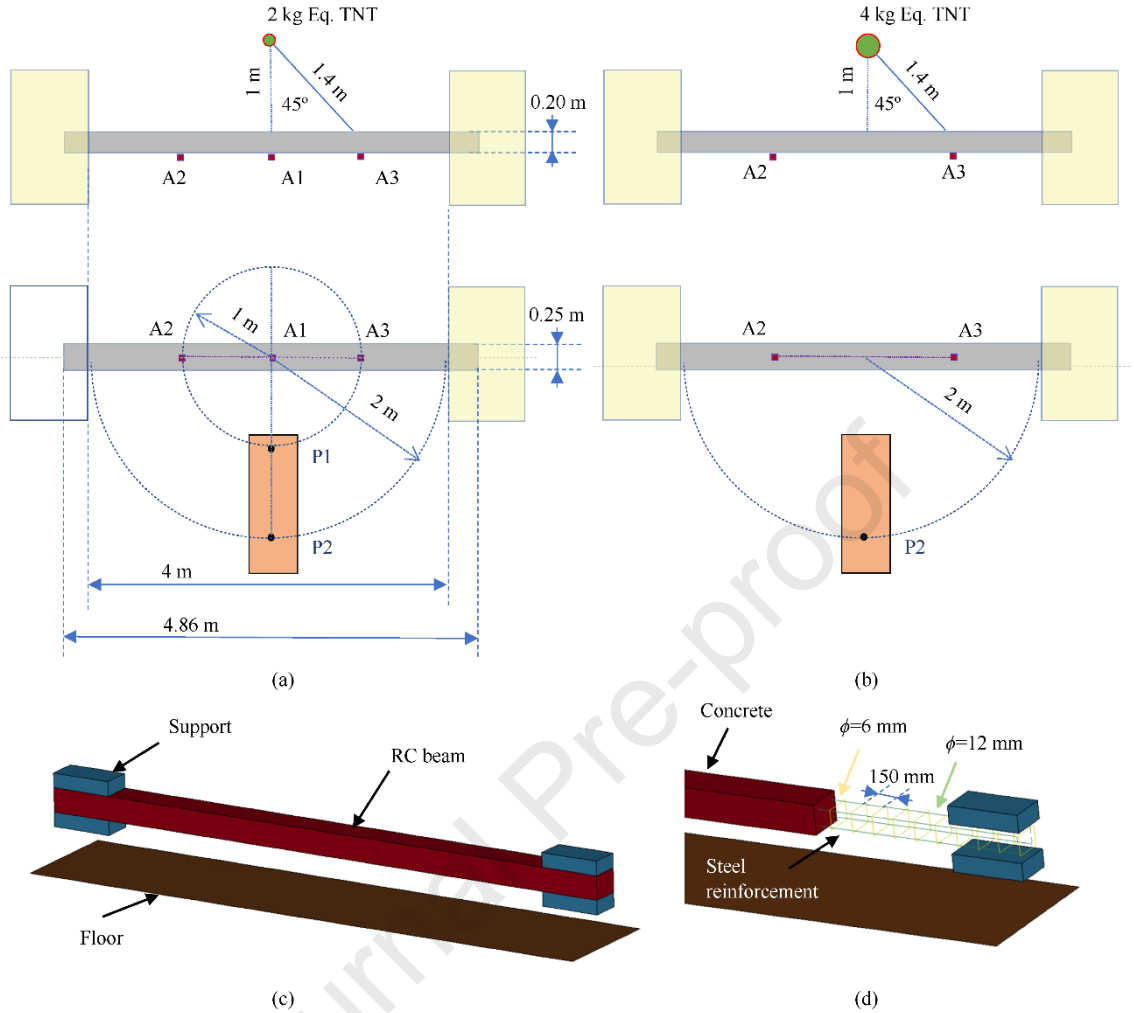

Fig. 2. Experimental set-up of structures: (a) Tested beams B1, B2 and B3; (b) Tested beam B4; (c) Numerical model overview; (d) Detail of the mesh reinforcement in the numerical model.

The dimensions of the beams were 4.86 meters in length, 0.25 meters in width, and 0.2 meters in depth (see Fig. 2). The main properties of the concrete used were a unit weight of 2300 kg/m^3, a compressive strength of 25 MPa, an aggregate size of 20 mm, a tensile strength of 3.7 MPa, an elastic modulus equal to 27.3 GPa and a Poisson ratio of 0.20. The steel rebars (B-500 S) had a unit weight equal to 7850 kg/m^3, a Young's modulus of 200 GPa, a Poisson's ratio of 0.30, a yield stress of 500 MPa, a tangent modulus equal to 1194 MPa and a plastic strain to failure of 0.12; following the UNE-EN 1992-1-1:2013 [39]. The concrete and steel used were the same as those used in the slab tests published in Castedo et al. [21]. The steel reinforcement consisted of four 12 mm diameter rebars along the length of the beams and located at their corners. There were also 6 mm diameter rebars placed every 150 mm, covering the entire length of the beams. In all cases the steel bars should be placed at about 30 mm from the external concrete surface, this data was measured with a magnetic probe metal detection equipment called Micro Covermeter by Kolectric Limited.

Positioned as shown in Fig. 2, a set of two ablative protected pressure transducers (P1, P2) and three accelerometers (A1, A2 and A3) were employed for the tests. In tests B1, B2 and B3 all the measuring sensors were used, while in the test B4 two pressure sensors and only two accelerometers were placed. Pressure transducers and accelerometers used in the trials were manufactured by PCB Piezotronics. All measuring devices were connected to a Nicolet Genesis multichannel data acquisition system that samples pressure and acceleration data at a rate of 500 kHz and 50 kHz, respectively. The other specimens (B5 and B6) were used to test the effect of the scaled distance on the beams and to compare the behavior of the numerical models developed and previously calibrated. In these last two tests and to prevent possible deterioration of the sensors due to the increase in the size of the load, no measuring sensors were used. In addition, all trials were recorded with a Photron Fastcam SA3-120k high-speed camera. It reaches a recording speed of 5000 images per second for a resolution of 512 × 512 pixels, reaching up to 120,000 fps for a resolution of 128 × 16 pixels. Also, the variation of the surface strength of the concrete after each detonation was measured by using a Schmidt hammer (model "Silver Schmidt" from Proceq). For details of the methodology and the results obtained with the Schmidt hammer the reader is referred to López et al. paper [40].

3. Numerical modelling

The adoption of finite element modeling is essential for comprehension, prediction, and simulation of the failure mechanisms and damage patterns in concrete structures subjected to extremely fast events such as blasts. In this work, for accurate representation, full-scale beams were 3D modelled and solved using a Lagrangian mesh with CONWEP data to replicate the pressure-time history produced by the explosive [41]. These numerical simulations were carried out using LS-DYNA Version 971-R14 [15]. Concrete was discretized using 3D solid elements, while the steel reinforcement was included as beam elements. The interaction between the concrete and steel elements has been performed using a penalty method (*Constrained_Lagrange_in_Solid), due to the different meshes used. This method constructs a system of constraints restricting the motion (in acceleration and velocity of the nodes) for both meshes to be consistent. The use of this methodology is acceptable as long as both materials work as a single set. This is the case in short duration and high-pressure events (such as an explosive phenomenon) since possible slippage or leakage between elements can be neglected [1,42]. In addition, the top and bottom of the supports where the beam is embedded are simulated (Figs. 1 and 2). In the upper areas of these supports, as well as in the lateral areas (including the concrete beam), the single point constraint (SPC) boundary condition is used, which cancels displacements and rotations in the relevant directions.

3.1. Blast loading

CONWEP data are incorporated into LS-DYNA by using the *Load_Blast_Enhanced or LBE function [15]. The empirical CONWEP data, basically the pressure-time curves, are applied on the target (beam in this case) face directly exposed to detonation. This technique can be used for a range of scaled distances between 0.15 and 40 m·kg$^{-1/3}$ and is therefore valid for all our tests (see Table 1). For its operation the module requires the equivalent mass of TNT (Table 1), the coordinates of the center of the charge with respect to the target (Table 1), the surface receiving the pressure wave (in this case the top surface) and the type of blast source (spherical free air blast).

3.2. Steel reinforcement

The steel rebars (properties in Section 2) are described in the simulation with an elasto-plastic model (namely in LS-DYNA: *Piecewise_Linear_Plasticity). The data input is minimal, and it responds very well to the behavior of the steels used as reinforcement, as demonstrated by its widespread use [30,42,43]. The stress-strain behavior has been considered with a bilinear curve by defining the tangent modulus. In this model, the deviatoric stresses (S_{ij}) satisfying the yield function (ϕ) are determined according to Eq.(1):

$$\phi = \frac{1}{2} S_{ij} S_{ij} - \frac{\left[\beta(\sigma_0 + f_h(\varepsilon_{eff}^p))\right]^2}{3} \leq 0 \quad (1)$$

being the expression inside the bracket the yield surface (σ_y) a function of the initial yield strength (σ_0). The linear hardening is obtained as follows: $f_h(\varepsilon_{eff}^p) = E_p(\varepsilon_{eff}^p)$; where E_p is the plastic hardening modulus ($E_p = EE_t/(E - E_t)$; with E and E_t are the Young's modulus and tangent modulus, respectively) and ε_{eff}^p is the effective plastic strain. The strain rate effects are considered with the Cowper-Symonds model: $\beta = 1 + (\dot{\varepsilon}/C)^{1/p}$; being $\dot{\varepsilon}$ the strain rate, C equal to 25.36 s^{-1} and p equal to 2.52. In all runs, the bar elements size was 10 mm in length, so the number of total beam elements were 4128.

3.3. Concrete

There are several types of material models for concrete implementation in LS-DYNA that have been successfully employed [44], some of them with reduced data input (i.e., KCC, CSCM, RHT) and others that require more information for operation (i.e., Johnson Holmquist Concrete – JHC or Winfrith). In this study, four different material models have been used and compared with the actual tests presented in Section 2. These materials have been: KCC, Winfrith, CSCM and RHT. The general form of the yield function for a pressure dependent material (like concrete) can be written as follows: $Y(I_1, J_2, J_3) = 0$; where I_1 is the first invariant of stress tensor (representing volumetric responses), J_2 and J_3 are the second and third invariants of deviatoric stress tensor (representing deviatoric responses). The way in which each numerical model incorporates these responses is what differentiates them.

The third evolution of the Karagozian & Case Concrete—KCC has found application in the comprehensive analysis of numerous reinforced concrete structures exposed to various loading

conditions, including quasi-static, blast, and impact scenarios [25]. This model uses three shear failure surfaces: yield strength (*y*), maximum strength (*m*), and residual strength (*r*), formulated in a generalized form as:

$$F_i(p) = a_{0i} + \frac{p}{a_{1i}+a_{2i}p} \tag{2}$$

where *i* stands for *y, m,* or *r*; *p* is the pressure $p = -I_1/3$; and a_{ji} (j = 0,1,2) are data automatically generated based on user input of density and unconfined compressive strength (see data in Section 2) [45]. The current failure surface is interpolated between the maximum strength surface and the yield strength surface or the residual strength surface as in Eq.(3):

$$F(I_1,J_2,J_3) = \begin{cases} r(J_3)\left[\eta(\lambda)(F_m(p) - F_y(p)) + F_y(p)\right] & \lambda \le \lambda_m \\ r(J_3)[\eta(\lambda)(F_m(p) - F_r(p)) + F_r(p)] & \lambda > \lambda_m \end{cases} \tag{3}$$

where λ is the modified effective plastic strain (or internal damage parameter) a function of J_2, damage evolution, pressure, strain rate enhancement factor—r_f (i.e. Dynamic Increase Factor—DIF) (see for more details: [46–48]). $r(J_3)$ is the scale factor in the form of William-Warnke equation [49]. In this model the strain rate enhancement (important to effectively capture high strain rate events such as close detonations) is introduced as the ratio of the enhanced strength value on the failure surface at pressure *P* versus the unenhanced one: $r_f = \Delta\sigma_e/\Delta\sigma$. The compressive and tensile strain rate effects are considered independently [46–48]. The interpolation function ($\eta(\lambda)$) is a function of λ with $\eta(0) = 0$ and $\eta(\lambda_m) = 1$, and $\eta(\lambda \ge \lambda_m) = 0$; being λ_m the maximum value of the internal damage parameter. For the damage definition, as the material moves from the yield strength surface to the maximum rupture surface the "scaled damage measure" ranges from 0 to 1; and then from the maximum rupture surface to the residual rupture surface the "scaled damage measure" varies from 1 to 2. This value is registered as the effective plastic strain in the LS-PrePost. This model is sometimes used together with the "ad-hoc" criterion of *MAT_ADD_EROSION [1,49] to simulate the erosion of concrete subjected to high strain rate loads. This is because the model does not incorporate a damage erosion criterion, as do other models such as CSCM.

The Winfrith model was developed and validated from the Broadhouse and Neilson experiments [50], with the intention of solving reinforced concrete structures subjected to impact loads. This model is based on a four-parameter plasticity model which has the plasticity portion based upon the shear failure surface as proposed by Ottosen [51]:

$$F(I_1,J_2,\cos 3\theta) = a\frac{J_2}{(f_c')^2} + \lambda\frac{\sqrt{J_2}}{f_c'} + b\frac{I_1}{f_c'} - 1 \tag{4}$$

$$\lambda = \begin{cases} k_1 \cos\left[\frac{1}{3}\cos^{-1}(k_2\cos 3\theta)\right] & \cos(3\theta) \ge 0 \\ k_1 \cos\left[\frac{\pi}{3} - \frac{1}{3}\cos^{-1}(-k_2\cos 3\theta)\right] & \cos(3\theta) < 0 \end{cases} \tag{5}$$

where θ is Lode angle ($\cos 3\theta = (3\sqrt{3}\,J_3)/(2\,J_2^{3/2})$); the constants a and b control the meridional shape of the shear failure surface; the constants k_1 and k_2 define the shape of shear failure surface in the octahedral (π-plane). The four constants are a function of the ratio between the unconfined compressive strength (f_c') and the unconfined tensile strength (f_t'). The model works with automatic parameter generation, provided that the user enters at least the uniaxial compression and uniaxial tension data (details in Section 2). It can simulate the softening of concrete under tension (accounting for factors like fracture energy and aggregate size) and can accommodate variations in strain rate. Strain rate enhancement is considered with a bilinear strain for "low" and "high" strain rate factors, recalculating f_c', f_t' and the Young's modulus [52]. When including the strain rate effects LS-DYNA uses the specific fracture energy to obtain the crack width, i.e. energy per unit area dissipated in opening a crack. The fracture energy G_f [N/m] is calculated using the equation $G_f = 73 \times f_c^{0.18}$ (see [53,54] for more details). If this expression is used and considering the value of the compressive strength in this case, a value of $G_f = 130$ N/m is obtained. This is in line with the values used by other researchers [19,55]. In this model, when the effective plastic deformation is represented in the LS-PrePost it corresponds to that same dimensionless variable but used as a damage parameter as Wu et al. [25].

The Continuous Surface Cap Model—CSCM was developed by the Federal Highway Administration (FHWA) to simulate the performance of road-side concrete barriers exposed to high dynamic loadings [56]. The CSCM employs a combination of shear (failure) surface with the hardening compaction surface (cap) by using a multiplicative formulation (that allows the smooth and continuous combination of the cap and shear surfaces at their intersection). The yield function is defined as follows:

$$f(I_1, J_2, J_3) = J_2 - \Re(J_3)^2 F_f^2(I_1) F_c(I_1, \kappa) \tag{6}$$

where $\Re(J_3)$ is the Rubin three-invariant decay coefficient, $F_f(I_1)$ is the shear failure surface (see Eq.(7)), and $F_c(I_1, \kappa)$ is the hardening cap with κ to be the cap hardening parameter (see Eqs.(8–10)).

$$F_f(I_1) = \alpha - \lambda \exp(-\beta I_1) + \theta I_1 \tag{7}$$

$$F_c(I_1, \kappa) = \begin{cases} 1 - \frac{(I_1 - L(\kappa))^2}{(X(\kappa) - L(\kappa))^2} & I_1 \geq L(\kappa) \\ 1 & I_1 \leq L(\kappa) \end{cases} \tag{8}$$

$$L(\kappa) = \begin{cases} \kappa & \kappa \geq \kappa_0 \\ \kappa_0 & \kappa \leq \kappa_0 \end{cases} \tag{9}$$

$$X(\kappa) = L(\kappa) + R F_f(I_1) \tag{10}$$

The expression corresponding to $I_1 \geq L(\kappa)$ in Eq.(8) represents the ellipse (or cap), which intersects the shear surface failure at $I_1 = L(\kappa)$. In addition, κ_0 is the value of I_1 at the initial intersection of the

cap and shear surfaces before the cap expands or shrinks. The cap expands ($X(\kappa)$ and κ increase) as compaction of the plastic volume occurs, whereas it contracts ($X(\kappa)$ and κ decrease) as expansion of the plastic volume occurs. Being $X(\kappa)$ the intersection between the cap hardening surface and the axis of I_1, with R the ellipticity ratio of the cap hardening surface. The movement of this cover is controlled by an isotropic hardening rule:

$$\varepsilon_{\mathrm{v}}^{p} = W\{1 - \exp(-D_1[X(k) - X_0] - D_2[X(k) - X_0]^2)\} \tag{11}$$

where the $\varepsilon_{\mathrm{v}}^{p}$ is the plastic volume strain, W is the maximum plastic volumetric strain, X_0 is the initial location of the cap when $\kappa = \kappa_0$. The LS-DYNA autonomously calculates the required dataset for defining this material (α, β, λ, θ, X_0, R, W, D_1 and D_2) by introducing some key parameters such as unconfined compressive strength, density, and maximum aggregate size (Section 2). The strain rate is based on the viscoplastic algorithm based on the Duvaut-Lions overstress formulation [57]. The strength calculation for the strain rate effect is based on the DIF (as KCC model) as the ratio between the dynamic strength (both compressive and tensile) of the concrete material to quasi-static strength. This model accounts for both strain softening and modulus reduction in a scalar damage parameter ranging from 0 to 1. When this parameter exceeds 0.99 in an element, and the maximum principal strain in the element surpasses the user-defined failure threshold (known as ERODE), that element is removed. In this research, the traditional ERODE value of 1.05 has been consistently applied [58]. This damage parameter is plotted in the LS-PrePost via the effective plastic strain.

The Riedel–Hiermaier–Thoma—RHT concrete model is widely employed to simulate the dynamic response of concrete structures when exposed to impulsive and blasting loads [59]. The elastic–plastic yield surface is described based on the compressive strength, the regularized yield function and the Willam-Warnke function as Eq.(12) [45].

$$\sigma_{\mathrm{y}}\left(P_0^*, \dot{\varepsilon}_{\mathrm{p}}, \varepsilon_{\mathrm{p}}^*\right) = f_{\mathrm{c}}\, \sigma_{\mathrm{y}}^*\left(P_0^*, F_{\mathrm{r}}, \varepsilon_{\mathrm{p}}^*\right) R_3(\theta, P_0^*) \tag{12}$$

where $\dot{\varepsilon}_{\mathrm{p}}, \varepsilon_{\mathrm{p}}^*$ are the strain rate and the effective plastic strain, respectively; f_{c} is the compressive strength parameter, σ_{y}^* is the normalized yield function [$\sigma_{\mathrm{y}}^*\left(P_0^*, F_{\mathrm{r}}, \varepsilon_{\mathrm{p}}^*\right) = \sigma_{\mathrm{f}}^*(P_0^*/\gamma\,, F_{\mathrm{r}})\gamma$ with $\gamma = \varepsilon_{\mathrm{p}}^* + (1 - \varepsilon_{\mathrm{p}}^*)F_{\mathrm{e}}F_{\mathrm{c}}$; being σ_{f}^* the failure surface—Eq.(13), F_{e} the elastic strength parameter and F_{c} the elliptical cap function of the yield surface similar to the CSCM model], P_0^* is the normalized pressure (ratio between hydrostatic pressure and f_c), F_{r} is a dynamic increment factor, R_3 is the Willam-Warnke function and θ denotes the Lode angle (given by the deviatoric stress tensor).

$$\sigma_{\mathrm{f}}^*(P_0^*, F_{\mathrm{r}}) = \begin{cases} A\left(P_0^* - F_{\mathrm{r}}/3 + (A/F_{\mathrm{r}})^{-1/n}\right)^n & 3P_0^* \geq F_{\mathrm{r}} \\ \frac{F_{\mathrm{r}} f_{\mathrm{s}}^*}{Q_1} + 3P_0^*\left(1 - \frac{f_{\mathrm{s}}^*}{Q_1}\right) & F_{\mathrm{r}} > 3P_0^* \geq 0 \\ \frac{F_{\mathrm{r}} f_{\mathrm{s}}^*}{Q_1} - 3P_0^*\left(\frac{1}{Q_2} - \frac{f_{\mathrm{s}}^*}{Q_1 f_{\mathrm{t}}^*}\right) & F_{\mathrm{r}} > 3P_0^* \geq 0 \\ 0 & 3P_{\mathrm{t}}^* \geq 3P_0^* \end{cases} \tag{13}$$

In this expression, A and n are failure surface parameters, f_{t}^* and f_{s}^* are the tensile and shear strength

of the concrete relative to f_c, Q values are introduced to account for the tensile and shear meridian dependence, and P_t^* is the failure cut-off pressure. In this model, as stress approaches the failure surface, a damage model, parametrized by plastic strain, governs the evolution of damage. This model effectively represents the post-failure stress limit surface by interpolating between the failure surface and the residual friction surface. It also incorporates a strain rate law with a dynamic increase factor (DIF) for tension, which varies with strain rates. The DIF is calculated as a ratio of the dynamic tensile strength relative to the static tensile strength. Some of the parameters used to obtain the DIF in this model follow experimental data given in CEB-FIB Model Code [57]. Notably, this model minimizes the number of input parameters, relying primarily on the unconfined compressive strength (see Section 2). In this work, following most publications using this model [7,24,60], the erosion criteria were set to default values, with the erosion parameter (eroding plastic strain— EPSF) scale factor equal to 2. The concrete elements are eroded when their effective plastic strain (plotted directly in the LS-PrePost) exceeds the value of EPSF parameter.

The selection of an optimal mesh size involves a delicate compromise between the requirements for accuracy and computational efficiency, especially considering the potential confinement of the concrete fracture progress zone (CFPZ) within a single mesh element in the numerical model. It is crucial to ensure that the mesh size does not exceed the dimensions of the CFPZ to prevent the loss of fracture energy. Conversely, a smaller mesh size could encompass multiple elements, potentially leading to increased damage [61]. For these reasons, three mesh sizes have been tested in all cases. The three sizes used have been 10, 15 and 20 mm implying a number of solids equal to 260,000, 73,593 and 32,500, respectively.

4. Results and discussion

Results from low mass explosive tests are shown first B1, B2 and B3, following by a description of test with beam B4, and finishing with the information extracted from beams B5 and B6.

As mentioned earlier, the first three trials (B1, B2 and B3) are used as calibration tests with low explosive mass (2 kg) at higher distance (1 m). Irrespective of the specific concrete material employed (KCC, Winfrith, CSCM, and RHT), the pressure exerted by the LBE technique exhibits uniform behavior across all cases. However, depending on the meshing, these values may change slightly due to the pressure log generated by the LBE tool. Therefore, the pressure applied to each element corresponding to one (P1) or two (P2) meters, in each case, is recorded. As can be seen in Fig. 3, these differences are negligible. For example, the values recorded for the peak pressure at P1 (1 m) for the numerical modelling are 4.12, 4.09 and 4.16 MPa for the 10, 15 and 20 mm meshes, respectively. The average value measured in tests B2 and B3 was 4.31 MPa, it should be noted that the sensor located at P1 for test B1 did not correctly register any signal and therefore, this data is discarded. The relative

differences as a function of meshing are 4.42%, 5.14%, and 3.53% for the 10, 15 and 20 mm meshes, respectively. In the case of sensor P2 (2 m), there are three signals corresponding to the three tests performed (Fig. 3), with average peak values equal to 0.49 MPa. In the simulations performed, for the 10 mm mesh the peak pressure is 0.47 MPa, for the 15 mm it is 0.46 MPa, and for the 20 mm the value is equal to 0.47 MPa. Therefore, the relative differences are 4.48% for the 10 and 20 mm meshes, and 6.51% for the 15 mm mesh. The numerical peak pressure values at P1 and P2 generally align with the experimental data, predominantly close to the lower bound, exhibiting a relatively small difference of approximately 5% in all cases. The numerical pressure decay at P1 closely corresponds to the experimental results. However, at P2, the numerical pressure decay occurs at a slower rate compared to the experimental traces, leading to higher impulse values (same as the previously published work [21].

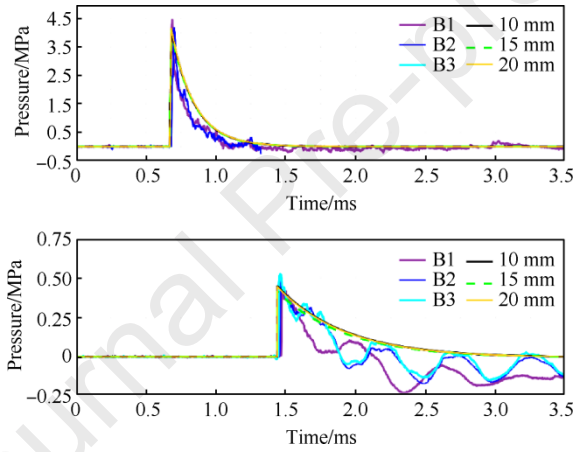

Fig. 3. Pressure-time signals for tests B1, B2 and B3. Upper: pressure at sensors P1 at 1 m vs signals simulated. Lower: pressure at sensors P2 at 2 m vs signals simulated. The legend is the same for upper and lower graphs.

The acceleration values comparing all the performed simulations and the measured one for the sensor A1 (Fig. 2) can be found in Table 2. The range of acceleration peaks measured in the three valid signals for tests B1, B2 and B3 at sensor A1 is wide and goes from 5.13×10^3 to 11.14×10^3 g. Regardless of the material model used, the 10 mm mesh size exceeds the peak acceleration value recorded in the tests. For this mesh size, the model that seems to fit best is Wintrith (Table 2), while KCC and CSCM show a very similar behavior, being RHT the one that seems to fit worst. For the rest of the grids and all the material models, the values are within the experimental range, although always close to the highest values. The KCC and CSCM models have a very similar behavior in all cases. The model developed with Winfrith presents systematically smaller acceleration values than the rest. On the contrary, the RHT model is the most affected in the peak acceleration values as a function of the meshing with a difference of 30%, while the rest have a difference of approximately 24%.

Table 2

Acceleration values for sensor located at A1 (see Fig. 2) in numerical models of beams B1, B2 and B3. If the acceleration registered with the model is within the measured limits in the field it is signalized with "wml", otherwise the relative difference is calculated by taking as reference the value measured at the extremes of the experimental range interval.

Material model	Mesh size /mm	Model acceleration/ ($\times 10^3$ g)	Difference/%
KCC	10	12.93	16.07
KCC	15	10.80	wml
KCC	20	9.84	wml
Winfrith	10	11.65	4.58
Winfrith	15	9.86	wml
Winfrith	20	8.86	wml
CSCM	10	12.95	16.25
CSCM	15	10.87	wml
CSCM	20	9.83	wml
RHT	10	13.85	24.33
RHT	15	10.96	wml
RHT	20	9.81	wml

Table 3 and Fig. 4 shows the acceleration values comparing all the performed simulations and field tests for the sensors A2/A3 (Fig. 2). In this case, from six possible signals, five were valid and one cannot be used as the register was not properly recorded. Due to the inherent heterogeneity of the tests, the signals do not necessarily have to be equal at positions A2/A3. In this case, they are considered equal when compared to the results of the model, which is symmetrical. The peak values in these signals vary from 0.89×10^3 to 2.64×10^3 g. Unsurprisingly, these values are well below those recorded by the sensors at the A1 position. The 10 mm meshes have differences of more than 40%. The 15 mm meshes for the KCC and CSCM models are around 5%, the RHT model reaches 12% and the Winfrith model shoots up to 30%. For the 20 mm meshing the KCC, CSCM and RHT models are within the measured ranges, while the Winfrith model has a small difference of 5%. In all cases a reduction in acceleration by approximately 36% can be observed for the 10 mm mesh to the 15 mm mesh. However, further increasing the mesh size to 20 mm shows a less substantial reduction of 22% compared to the 15 mm mesh. This pattern suggests a potential diminishing effect of mesh size on acceleration beyond a certain threshold. The acceleration signals extracted from the 10 mm models show similar damping to that recorded in the tests (see Fig. 4), but as mentioned above, the peak values are too high. In the others, the values are more in accordance with the records, especially the 15 mm mesh which describes better the damping of the wave. However, in the case of 20 mm, the accelerations of the models have a peak in accordance with that recorded, but a somewhat fast damping. It is possible that this is due to the size of the aggregate which in this case is also 20 mm, the study of

this possible correlation is an open avenue for future research.

Table 3

Acceleration values for sensors located at A2/A3 (see Fig. 2) in numerical models of beams B1, B2 and B3. If the acceleration registered with the model is within the measured limits in the field it is signalized with "wml", otherwise the relative difference is calculated by taking as reference the value measured at the extremes of the experimental range interval.

Material model	Mesh size /mm	Model acceleration/ ($\times 10^3$ g)	Difference /%
KCC	10	4.42	40.27
KCC	15	2.80	5.71
KCC	20	2.23	wml
Winfrith	10	6.04	56.29
Winfrith	15	3.78	30.16
Winfrith	20	2.78	5.04
CSCM	10	4.39	39.86
CSCM	15	2.75	4.00
CSCM	20	2.04	wml
RHT	10	4.67	43.47
RHT	15	3.01	12.29
RHT	20	2.34	wml

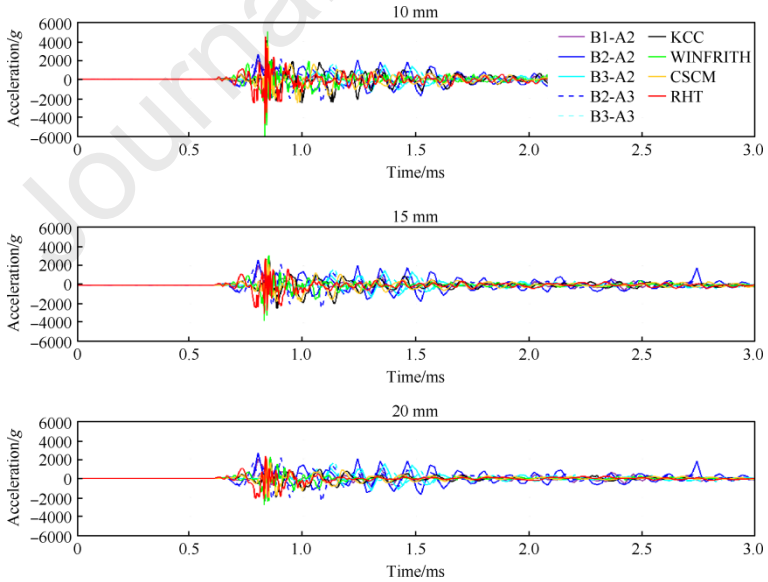

Fig. 4. Acceleration values corresponding to the locations A2/A3 in tests B1, B2 and B3 showing the differences between concrete models (see Table 3).

The detail of the damaged or affected areas can be seen in Fig. 5 for beam B2. Beams B1 and B3 presented a very similar result. There is no image of the beam at the top after the test, as there was no damage, not even some small transverse cracks as seen in the lower part of Fig. 5. This is quite common in RC tests against low load explosions at this distance [10,11]. The KCC model shows

excessive damage with numerous zones with a value close to 2, as is the case in other publications [1,32]. Although the deformation values of the Winfrith model are very low, they are concentrated in the center of the beam with deformations towards the sides in a concentric manner. However, the CSCM and RHT models show a better appearance of the affected areas with a much more localized zone. The maximum displacement has been measured as the difference in the position of the top face of the beam at the lowest point after detonation versus its original position before detonation. This has been done by adjusting and calibrating the images, as they were not measured in the field at the time of testing. For beams B1-B3, no displacement of the beam is observed after the tests. The same is true for the three meshes tested for each of the four concrete models used in the simulation.

Fig. 5. On the top, field test photo corresponds with the bottom part of the beam B2 tested and high-speed video frame of the detonation. Bottom view of the beam models corresponding to the 15 mm meshes. Legends show the effective plastic strain of the concrete model of the beam.

In the case of beam B4, the pressure measured at sensor P2 (2 m) was 0.33 MPa, while the numerical model values were 0.75 MPa for the 10 and 20 mm meshes, and a value of 0.74 for the 15 mm mesh. The relative differences are 2.60% and 3.90%, respectively. In all cases the applied values are quite close to those recorded in the tests (Fig. 6). The pressure on the P1 (1 m) measured in the simulation was 7.81 MPa for the 10 mm model, 7.76 MPa for the 15 mm and 7.86 MPa for the 20 mm. These values cannot be validated, as no measurements were performed in the test.

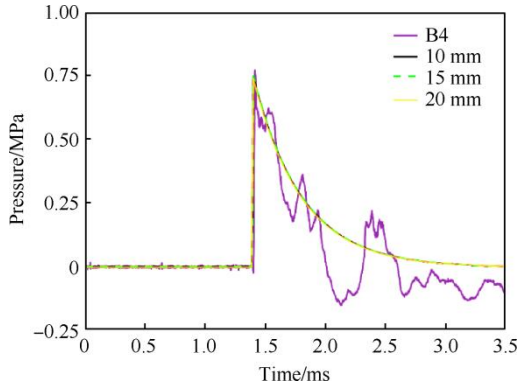

Fig. 6. Pressure vs Time signal recorded and simulated for test B4 at sensor P2 located at a distance of 2 m.

In the B4 beam test, the two possible signals were recorded with peaks ranging from 2.1×10^3 to 4.8×10^3 g. As expected, these accelerations are generally larger than in the previous case with 2 kg of TNT equivalent. The same happens with the numerical results as shown in Table 4 and Fig. 7. The Winfrith shows a similar behavior as before with biggest difference in acceleration related with the mesh size effect. KCC and CSCM exhibit a similar behavior as the mesh size increases, the acceleration tends to decrease gradually. Again, the RHT model tends to overestimate the accelerations in two of the three grids. In fact, if the average of the differences of each model is calculated for each grid, it can be observed that the KCC and CSCM models perform similarly with a value of 12.5% and 14.7% respectively (in accordance with Castedo et al. [1]). In the Winfrith model this value rises to 23.4% and reaches 26.3% for the RHT model. Fig. 7 shows that all the signals of the models present a damping according to what was recorded in the field. This variability in the recorded signals also demonstrates the difficulty and importance of data collection in full-scale tests.

Table 4

Acceleration values for sensors located at A2/A3 (see Fig. 2) in numerical models of beams B4. If the acceleration registered with the model is within the measured limits in the field it is signalized with “wml”, otherwise the relative difference is calculated by taking as reference the value measured at the extremes of the experimental range interval.

Material model	Mesh size/ mm	Model acceleration/ ($\times10^3$ g)	Difference/ %
KCC	10	5.17	7.71
KCC	15	4.87	1.46
KCC	20	3.15	wml
Winfrith	10	6.92	44.17
Winfrith	15	4.72	wml
Winfrith	20	2.89	wml
CSCM	10	5.78	20.42
CSCM	15	4.68	wml
CSCM	20	3.55	wml
RHT	10	6.48	35.00
RHT	15	5.98	24.58

RHT	20	4.48	wml

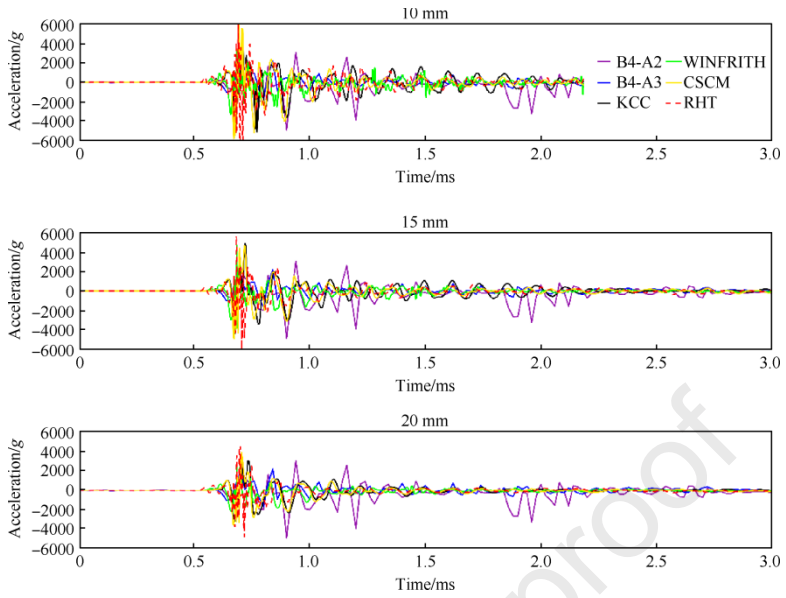

Fig. 7. Acceleration values corresponding to the locations A2/A3 in test B4 showing the differences between concrete models (see Table 4).

As can be seen in Fig. 8, on the bottom face of the beams, the effect of the detonation was more important on the bottom face than on the top face. However, in the KCC model the damage is still significant, much more than that seen in the real test on both sides. The Winfrith model, although it moves up the scale for effective plastic strain, still has a centered and concentric type of deformation on the bottom part that is not seen in the test. There is hardly any damage to the upper face. Again, it seems that the CSCM and RHT models show good results on the bottom face, especially the former which follows an affected pattern perpendicular to the main dimension of the beam as in the trial. However, on the upper face, the CSCM model shows damage towards the embedment's, while the RHT model shows only two small deformations in the central area. As in the previous beams, increasing the load from 2 kg to 4 kg does not affect the maximum displacement, which remains zero in both the test and the model.

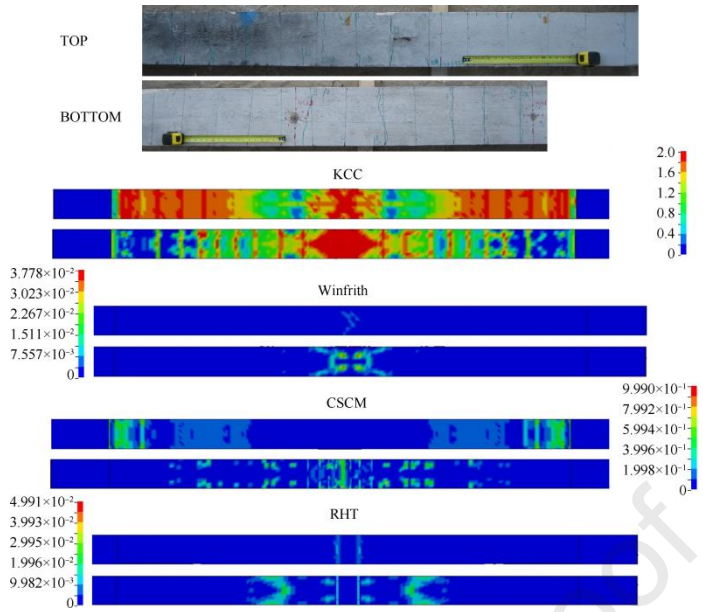

Fig. 8. Field test photos correspond with the top and bottom part of the beam B4 tested. Top and bottom view of the beam models corresponding to the 20 mm meshes. Legends show the effective plastic strain of the concrete model of the beam.

In beam B5 (Fig. 9) there was a central failure with some erosion and cracking in the lower part of the beam, as well as in the sides. With the load used at one meter, a karate chop type breakage of the beam occurs, an effect that is observed for the same conditions in other structures such as slabs [62]. As no images of the bottom face are available, since in the disassembly of the beam it was struck and broken, only the lateral openings are considered for comparison with the numerical models (Table 5). In this test, beam displacements are observed, and the measurements are also presented in Table 5. A non-clear pattern is observed in the damage length and deformation in the models as the mesh size changes, indicating the differences in the behavior of the model at different geometric resolutions and the importance of studying them. The KCC model has always bigger damage than the reference value from 1.2% for the 10 mm mesh up to 1.9% for the 20 mm one. However, as the size of the mesh elements increases the maximum deformation decreases. In this case the 20 mm model would be the closest to what was measured in the test. The Winfrith model shows marked erosion in the center and as the mesh increases, "random" eroded elements appear. This model systematically underestimates the damage length values; on the contrary, it tends to overestimate the deformation values. Again, the mesh equal to 20 mm present the best result in terms of maximum deformation. The CSCM is the one that describes the damage more realistically (in accordance with previous works [21,63]), with the biggest difference of just –0.6% for the 10 mm grid. Once again, this model has a smaller maximum deformation as the mesh increases, but in this case the best mesh is 10 mm. Finally, the RHT model overestimates the eroded elements for the small and big meshes but underestimate it for the other one. In general, this model is the one that presents the greatest differences with the test in the set of the

three grids for both parameters. Also, as shown in Fig. 9, it presents numerous fractures along the structural element. This behavior is not observed in the tested beam B5. In general, the models can capture the damage length better than the maximum deformation, a fact that may also be influenced by the simulation of the supports.

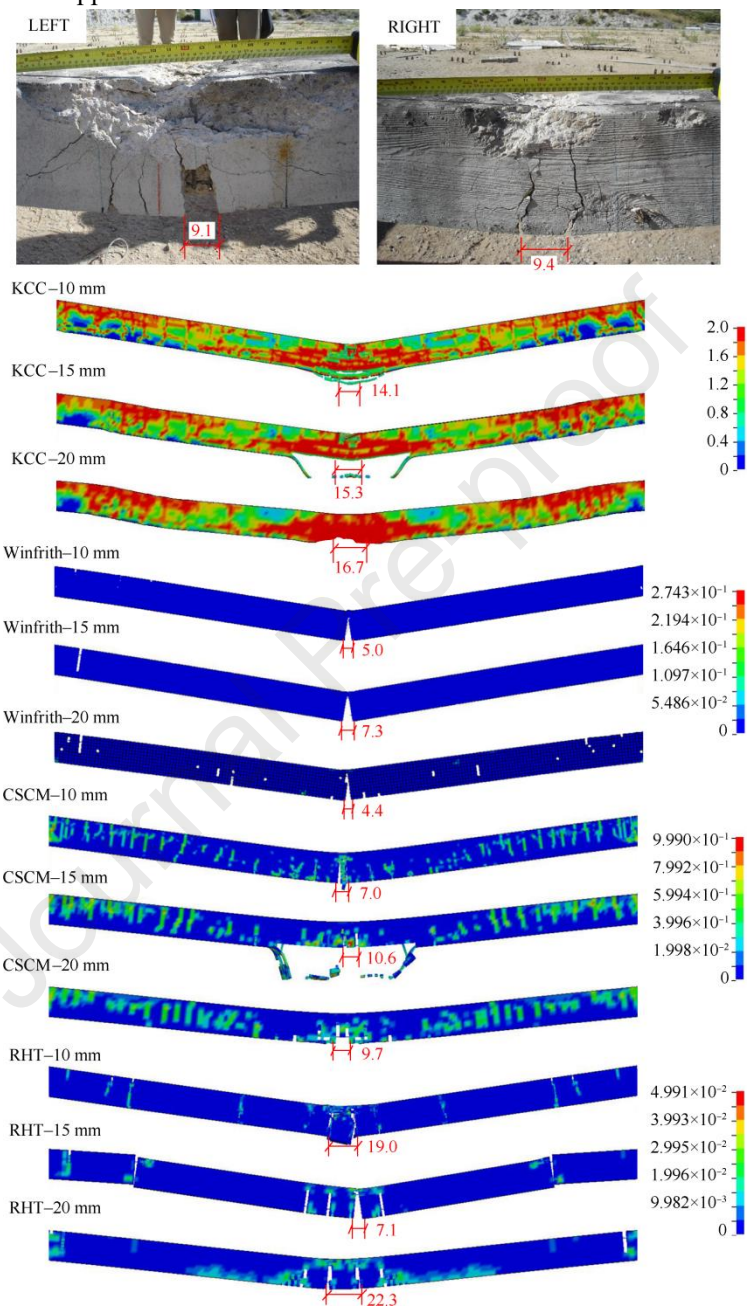

Fig. 9. Field test photos correspond with the left and right side of the beam B5 tested. Lateral view of all beam models with all meshes, the vertical-colored lines in the models show the measured damage size, see Table 5 with data. The legends show the effective plastic strain. Lengths are marked in cm.

Table 5

Length of damage and maximum deformation measured and simulated in beam B5. The damage size of the test is estimated as the average between two measurements 9.1 and 9.4 (see Fig. 9). The total

length considered is the beam span that is 400 cm (see Fig. 2).

Model	Mesh size /mm	Damage length /cm	Percentage over total /%	Damage Dif. test vs. model /%	Max. Deformation /cm	Deformation Dif. test vs. model /%
Test B5	–	9.25	2.3	–	11.9	–
KCC	10	14.1	3.5	1.2	15.1	26.9
KCC	15	15.3	3.8	1.5	13.4	12.6
KCC	20	16.7	4.2	1.9	11.3	–5.0
Winfrith	10	5.0	1.3	–1.1	15.2	27.7
Winfrith	15	7.3	1.8	–0.5	16.0	34.5
Winfrith	20	4.4	1.1	–1.2	12.3	3.4
CSCM	10	7.0	1.8	–0.6	12.7	6.7
CSCM	15	10.6	2.7	0.3	9.5	–20.2
CSCM	20	9.7	2.4	0.1	9.0	–24.4
RHT	10	19.0	4.8	2.4	13.6	14.3
RHT	15	7.1	1.8	–0.6	13.6	14.3
RHT	20	22.3	5.6	3.3	9.8	–17.6

Beam B6 with 15 kg of explosive at 0.5 m shows significant local damage, perforating and pulverizing the concrete in the central area (Fig. 10 and Table 6). The KCC and CSCM models tend to reproduce this type of breakage in a fairly similar manner obtaining analogous differences for the damage area and the maximum deformation. Although the damage lengths differ, with larger values in the KCC model for the 10 and 15 mm meshes. Not so with the 20 mm model whose values are closer to the measured. The maximum difference in terms of damaged area is 10%, with a mean value for all meshes of 5.7% (if the absolute value is considered, the average value rises to 8%). Also, it should be noted that this model presents a great difference between meshes for lateral damage and maximum deformation (Table 6). The CSCM is not as affected by the change in meshing and although it underestimates the damage lengths, the overall appearance is good. The mean difference of all meshes with respect to the lateral area of damage measured in the test is –9.6%. However, the CSCM tends to overestimate the maximum measured deformations. The Winfrith, as was the case for the B5 beam, systematically underestimates the damage length and so the lateral area with a mean value for the three meshes equal to –17.6%. In addition, this model shows numerous fractures along the beam, which is not seen in the test. The same is true for the maximum deformation which this model is not able to reproduce with a significant difference. The RHT model, like the CSCM and Winfrith, hardly varies depending on the meshing, presenting damage lengths like those measured in the field. This is reflected in the fact that the lateral damage area values are the smallest of all the models with an average value equal to 0.7% (or 1.4% in absolute values). This behavior does not hold if the maximum deformation is observed. For this parameter, the difference between the 10 mm and 15/20 mm meshes is at least 10 cm. However, it is the model with the lowest mean error against maximum deformation, followed by the KCC and the CSCM. On the other hand, this model does not reproduce the shape of

the damage very well, since it presents complete fractures along the beam, which produces a "chopping" of the beam. In test B6 the differences between models and test may also be due to excessive movement of the supports which is not reproduced in the model, see Fig. 10.

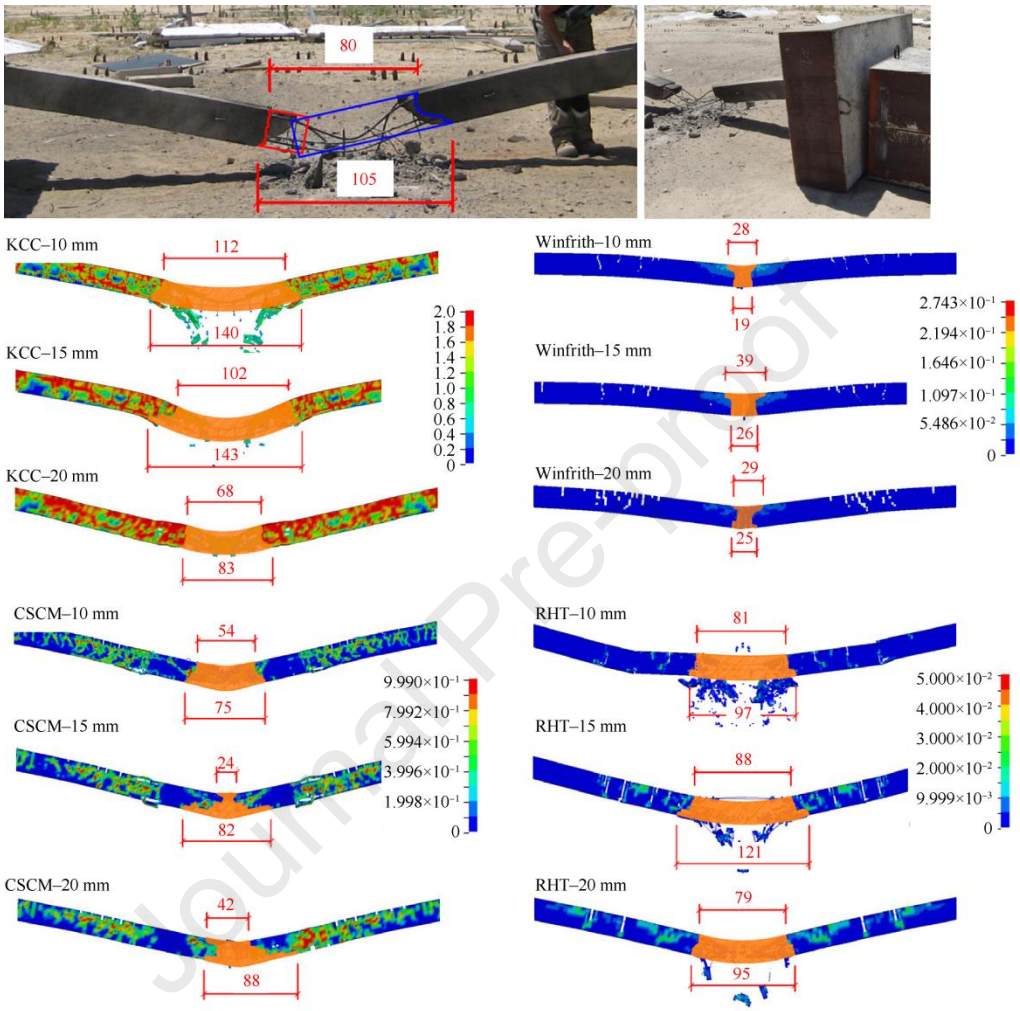

Fig. 10. Photograph of the B6 beam and models with all meshes. Lengths are marked in cm. The legends show the effective plastic strain of each concrete model.

Table 6

Lateral damage area and maximum deformation for beam B6. Note that the lateral area of the beam is 8000 cm^2.

Model	Mesh size /mm	Damage area /cm^2	Percentage over total /%	Difference test vs. model /%	Max. Deformation /cm	Deformation Dif. test vs. model /%
Test B6	–	1880	23.5	–	37.7	–
KCC	10	2706	33.8	10.3	34.8	–6.7
KCC	15	2699	33.7	10.2	45.5	22.0
KCC	20	1594	19.9	–3.6	41.5	11.3
Winfrith	10	402	5.0	–18.5	12.8	–65.7
Winfrith	15	573	7.2	–16.3	12.0	–67.8
Winfrith	20	439	5.5	–18.0	20.8	–44.2

CSCM	10	1343	16.8	–6.7	42.8	14.7
CSCM	15	783	9.8	–13.7	43.0	15.3
CSCM	20	1205	15.1	–8.4	41.1	10.2
RHT	10	1854	23.2	–0.3	31.2	–16.4
RHT	15	2134	26.7	3.2	42.6	14.2
RHT	20	1828	22.9	–0.6	41.3	10.7

5. Conclusions

Six full-scale reinforced concrete beam tests were carried out to analyze their resistance to near blast at different scaled distances ranging from 0.2 to 0.8 m·kg$^{-1/3}$. In addition, 48 Lagrangian simulations with LBE have been carried out in the LS-DYNA program, combining the use of four models for concrete (KCC; Winfrith, CSCM, and RHT) with three different meshes (10, 15 and 20 mm).

From the full-scale tests, it can be extracted that the beams subjected to low loads (2 and 4 kg of TNT equivalent) at one meter do not show significant damage, especially on the face exposed to detonation. However, the accelerations to which they are subjected do have some importance, so that a study of the interior of the material after a blast event would be advisable for future work. When the distance is maintained, and the load is increased to 15 kg TNT equivalent, very local damage occurs, especially on the bottom side of the beam. In this case, the beam bent through a linear fracture along its minor axis of symmetry. With the same load and reducing the distance to half a meter, there is a significant perforation in the central area of the beam that reaches one meter in length.

Simulations often capture general patterns but may overestimate or underestimate specific measurements such as damage length, area, or maximum displacement. For example, the KCC model tends to overestimate these parameters, conversely the Winfrith model tends to underestimate them, while the CSCM and RHT models tend to be less variable. However, in terms of break shape or pattern the KCC and CSCM models are the most reliable. As expected, the differences in all recorded pressures according to the meshing are minimal since it depends on the position of the elements. These values do not change between models. If the measured accelerations are compared, the simulations match the experimental values well. However, there are discrepancies, especially for the 10 mm mesh size, where some models, such as Winfrith and RHT, show higher peak acceleration values compared to the experimental records. When the mesh becomes coarser (20 mm), the accelerations in all models and meshes tend to reduce coinciding with the ranges measured in the tests.

There is a complex and nonlinear relationship between material models, mesh size and their effects on acceleration measurements or on model damage and size. Although there are factors that have not been studied here and are critical such as steel bars distribution, wrapping of beams, grain size of aggregates or eventual fibers in concrete able to increase toughness. The results obtained in

this research reflect the importance of understanding the mutual interaction of as many factors as possible. This is especially important when using models without tests to compare or calibrate against, as the results may be misinterpreted.

6. References

[1] Castedo, R., Santos, A. P., Alañón, A., Reifarth, C., Chiquito, M., López, L. M., Martínez-Almajano, S. & Pérez-Caldentey, A. Numerical study and experimental tests on full-scale RC slabs under close-in explosions. Eng. Struct.2021; 231, 111774.

[2] Zhao, C., Wang, Q., Lu, X., Huang, X., & Mo, Y. L. Blast resistance of small-scale RCS in experimental test and numerical analysis. Eng. Struct., 199, 2019; 109610.

[3] Bermejo, M., Santos, A. P., & Goicolea, J. M. Development of practical finite element models for collapse of reinforced concrete structures and experimental validation. Shock Vib., 2017.

[4] Xiao, W., Andrae, M., Steyerer, M., & Gebbeken, N. Investigations of blast loads on a two-storeyed building with a gable roof: Full-scale experiments and numerical study. J. Build. Eng., 2021; 43, 103111.

[5] Santos, A. P., Castedo, R., López, L. M., Chiquito, M., Yenes, J. I., Alañón, A., E. Costamagna & Martínez-Almajano, S. Reinforced Concrete Building with IED Detonation: Test and Simulation. Applied Sciences, 2022; 12(15), 7803.

[6] Ruggiero, A., Bonora, N., Curiale, G., De Muro, S., Iannitti, G., Marfia, S., Sacco, E. Scafati, S., & Testa, G. Full scale experimental tests and numerical model validation of reinforced concrete slab subjected to direct contact explosion. Int. J. Impact Eng., 2019; 132, 103309.

[7] Castedo, R., Santos, A. P., Chiquito, M., López, L. M., Pérez-Caldentey, A., Martínez-Almajano, S. & Alañon, A. Numerical and experimental study of externally reinforced RC slabs using FRPs subjected to close-in blast loads. Int. J. Impact Eng., 2021; 156, 103939.

[8] Chen, L., Fang, Q., Hong, J., Liu, Z. X., & Xiang, H. B. Dynamic responses of reinforced concrete beams under double-end-initiated close-in explosion. Def. Technol., 2018; 14(5), 527-539.

[9] Karayannis, C. G., & Golias, E. Full-scale experimental testing of RC beam-column joints strengthened using CFRP ropes as external reinforcement. Eng. Struct., 2022; 250, 113305.

[10] Lukić, S., & Draganić, H. Blast Loaded Columns—State of the Art Review. Applied Sciences, 2021; 11(17), 7980.

[11] Anas, S. M., Alam, M., & Umair, M. Experimental and numerical investigations on performance of reinforced concrete slabs under explosive-induced air-blast loading: A state-of-the-art review. Structures, 2021; 31, 428-461.

[12] Zhang, C., Gholipour, G., & Mousavi, A. A. Blast loads induced responses of RC structural members: State-of-the-art review. Composites, Part B, 2020; 195, 108066.

[13] Alshaikh, I. M., Bakar, B. A., Alwesabi, E. A., & Akil, H. M. Experimental investigation of the progressive collapse of reinforced concrete structures: An overview. Structures, 2020; 25, 881-900.

[14] ANSYS. AUTODYN User Manual Version 15.0 2013.

[15] ANSYS. LS-DYNA Keyword User´s Manual Vol. I – R14, 2023; 3968.

[16] Su, Q., Wu, H., & Fang, Q. Calibration of KCC model for UHPC under impact and blast loadings. Cement and Concrete Composites, 2022; 127, 104401.

[17] Shi, Y., Hu, Y., Liu, S., Cui, J., & Chen, L. Mitigation of the blast load on RC column by hanging granite slabs. Eng. Struct., 2023; 280, 115668.

[18] Thai, D. K., Nguyen, D. L., Pham, T. H., & Doan, Q. H. Prediction of residual strength of FRC columns under blast loading using the FEM method and regression approach. Constr. Build. Mater, 2021; 276, 122253.

[19] López, L. M., Pérez-Caldentey, A., Santos, A. P., Diego, Y. G., Castedo, R., & Chiquito, M. Experimental response and numerical modelling of a full-scale two-span concrete slab frame subjected to blast load. Eng. Struct., 2023; 296, 116969.

[20] Lee, M., & Kwak, H. G. Numerical simulations of blast responses for SFRC slabs using an orthotropic model. Eng. Struct., 2021; 238, 112150.

[21] Castedo, R., Segarra, P., Alañon, A., Lopez, L. M., Santos, A. P., & Sanchidrian, J. A. Air blast resistance of full-scale slabs with different compositions: Numerical modeling and field validation. Int. J. Impact Eng., 2015; 86, 145-156.

[22] Liu, C., Liu, J., Wei, J., Xu, S., & Su, Y. Parametric Study on Contact Explosion Resistance of Steel Wire Mesh Reinforced Geopolymer Based Ultra-High Performance Concrete Slabs Using Calibrated Continuous Surface Cap Model. Buildings, 2022; 12(11), 2010.

[23] Wu, J., Zhou, Y., Zhang, R., Liu, C., & Zhang, Z. Numerical simulation of reinforced concrete slab subjected to blast loading and the structural damage assessment. Eng. Fail. Anal., 2020; 118, 104926.

[24] Zhao, L., Hao, Y., Wang, Q., Yang, C., Yao, H., & Jia, X. Damage Zone of the Reinforced Concrete Beam under Rectangular Explosive Contact Explosions. Buildings, 2023; 13(6), 1403.

[25] Wu, Y., Crawford, J. E., & Magallanes, J. M. Performance of LS-DYNA concrete constitutive models. In 12th International LS-DYNA users conference, 2012; (Vol. 1, pp. 1-14).

[26] Maazoun, A., Matthys, S., Belkassem, B., Lecompte, D., & Vantomme, J. Blast response of retrofitted reinforced concrete hollow core slabs under a close distance explosion. Eng. Struct., 2019; 191, 447-459.

[27] Mahdavi Talaromi, H., & Sakhaee, F. Evaluation and comparison of concrete constitutive models in numerical simulation of reinforced concrete slabs under blast load. Int. J. Prot. Struct., 2022; 13(1), 80-98.

[28] Hussein, A., Heyliger, P., & Mahmoud, H. Blast response of a thin oriented strand board wall. Eng. Struct., 2019; 201, 109835.

[29] Patel, M., & Patel, S. Novel design of honeycomb hybrid sandwich structures under air-blast. J Sandw Struct Mater, 2022; 24(8), 2105-2123.

[30] Dua, A., Braimah, A., & Kumar, M. Influence of Standoff Distance on the Response of RC Columns Subjected to Close-In Explosions. J. Struct. Eng., 2022; 148(6), 04022068.

[31] Xiao, W., Andrae, M., & Gebbeken, N. Numerical study of blast mitigation effect of innovative barriers using woven wire mesh. Eng. Struct., 2020; 213, 110574.

[32] Wang, Z., Chen, W., Hao, H., Dong, Y., & Huang, Z. Numerical prediction of blast fragmentation of reinforced concrete slab using ALE-FEM-SPH coupling method. Finite Elem. Anal. Des., 2023; 220, 103948.

[33] Karmakar, S., & Shaw, A. Response of RC plates under blast loading using FEM-SPH coupled method. Eng. Fail. Anal., 2021; 125, 105409.

[34] Saifi, F., Haris, M., Tahzeeb, R., Shariq, M., Alam, M., & Anas, S. M. A coupled SPH-FEM analysis of explosion-induced blast wave pressure on thin-walled cylindrical steel liquid storage tank and corresponding structural response. Int. J. Masonry Res. Innov. 2023.

[35] Janota, O., & Foglar, M. Experimental and Numerical Evaluation of UHPFRC Slabs Subjected to Contact and Close-in Explosion. Sol St Phen, 2020; 309, 180-185.

[36] Hilding D. Methods for modelling Air blast on structures in LS-DYNA. Nord. LS-DYNA Users' Conf., Gothenburg, Sweden: 2016; p. 65.

[37] Casarrubios-Gómez, V. Cálculo del equivalente TNT de diversos explosivos. Proyecto Fin de Grado en la ETSI de Minas y Energía, Universidad Politécnica de Madrid. https://oa.upm.es/51755/, 2018.

[38] UFC 3-340-02. Structures to resist the effects of accidental explosions. US Department of the Army, Navy and Air Force Technical Manual; 2008.

[39] UNE-EN 1992-1-1:2013: Eurocode 2: Design of concrete structures - Part 1-1: General rules and rules for buildings 2013.

[40] López, L. M., Castedo, R., Chiquito, M., Segarra, P., Sanchidrián, J. A., Santos, A. P., & Navarro, J. Post-blast non-destructive damage assessment on full-scale structural elements. J. Nondestr. Eval., 2019; 38(1), 30.

[41] Hyde, D.W. Microcomputer Programs CONWEP and FUNPRO, Applications of TM 5-855-1,'Fundamentals of Protective Design for Conventional Weapons' (User's Guide); No. WES/IR.; ARMY ENGINEER WATERWAYS EXPERIMENT STATION VICKSBURG MS STRUCTURES LAB., 1988.

[42] Fang, C., Yosef, T. Y., & Linzell, D. G. Multi-Hazard-Resistant Behavior of CFRP-and Polyurea-Retrofitted Reinforced Concrete Two-Column Piers under Combined Collision–Blast Loading. Materials, 2023; 16(10), 3784.

[43] Wang, L. J., Wang, T., Cheng, S., Yin, W. J., & Liao, Z. Difference Analysis of Different Explosion Load Simulation Methods Based on LS-DYNA. In J. Phys. Conf. Ser. 2023; Vol. 2478, No. 7, p. 072053. IOP Publishing.

[44] Abedini, M., & Zhang, C. Performance assessment of concrete and steel material models in ls-dyna for enhanced numerical simulation, a state of the art review. Arch. Comput. Methods Eng., 2021; 28, 2921-2942.

[45] ANSYS. LS-DYNA Keyword User´s Manual Vol. II – Material Models, 2023, 2149.

[46] Malvar, L. J., Crawford, J. E., Wesevich, J. W., & Simons, D. A plasticity concrete material model for DYNA3D. Int. J. Impact Eng., 1997; 19(9-10), 847-873.

[47] Magallanes, J. M., Wu, Y., Malvar, L. J., & Crawford, J. E. Recent improvements to release III of the K&C concrete model. In 11th international LS-DYNA Users conference, 2010; Vol. 1, No. 3, pp. 37-48. Livermore Software Technology Corporation Livermore, CA.

[48] Crawford, J. E., Magallanes, J. M., Lan, S., & Wu, Y. User's manual and documentation for release III of the K&C concrete material model in LS-DYNA. Technical Rep., 2011; TR-11-36, 1.

[49] Zhao, M. Z., Lehman, D. E., & Roeder, C. W. (2021). Modeling recommendations for RC and CFST sections in LS-Dyna including bond slip. Eng. Struct. 229, 111612.

[50] Broadhouse, B. J., & Neilson, A. J. Modelling reinforced concrete structures in DYNA3D (No. AEEW-M-2465). UKAEA Atomic Energy Establishment, 1987.

[51] Iwalekar, A. A. Finite element analysis and experimental validation of reinforced concrete single-mat slabs subjected to blast loads. Master Thesis, University of Missouri, Kansas City, 2018; pp. 111. https://hdl.handle.net/10355/67037.

[52] Schwer, L. (2010). An introduction to the Winfrith concrete model. Schwer Engineering & Consulting Services, 1-28.

[53] Rubin, M. B. Simple, convenient isotropic failure surface. J. Eng. Mech., 1991; 117(2), 348-369.

[54] Code, M. FIB model Code for concrete structures. Struct. Concr., 2013; 14.

[55] Arano, A., Colombo, M., Martinelli, P., Øverli, J. A., Hendriks, M. A., Kanstad, T., & Di Prisco, M. Material characterization approach for modeling high-strength concrete after cooling from elevated temperatures. J. Mater. Civ. Eng., 2021; 33(5), 04021086.

[56] Murray, Y. D. User's manual for LS-DYNA concrete material model 159 (No. FHWA-HRT-05-062). United States. Federal Highway Administration. Office of Research, Development, and Technology, 2007.

[57] Brannon, R. M., & Leelavanichkul, S. Survey of four damage models for concrete. Sandia National Laboratories, 2009; 32(1), 1-80.

[58] Murray, Y. D., Abu-Odeh, A. Y., & Bligh, R. P. Evaluation of LS-DYNA concrete material model 159 (No. FHWA-HRT-05-063). United States. Federal Highway Administration. Office of Research, Development, and Technology, 2007.

[59] Riedel, W. 10 years RHT: A review of concrete modelling and hydrocode applications. Predictive Modeling of Dynamic Processes: A Tribute to Professor Klaus Thoma, 2009; 143-165.

[60] Grunwald, C., Schaufelberger, B., Stolz, A., Riedel, W., & Borrvall, T. A general concrete model in hydrocodes: verification and validation of the Riedel–Hiermaier–Thoma model in LS-DYNA. Int. J. Prot. Struct., 2017; 8(1), 58-85.

[61] Alañón, A., Cerro-Prada, E., Vázquez-Gallo, M. J., & Santos, A. P. Mesh size effect on finite-element modeling of blast-loaded reinforced concrete slab. Eng. Comput., 2018; 34, 649-658.

[62] Chiquito, M., López, L. M., Castedo, R., Santos, A. P., & Pérez-Caldentey, A. Full-Scale Field Tests on Concrete Slabs Subjected to Close-In Blast Loads. Buildings, 2023; 13(8), 2068.

[63] Gomathi, K. A., Rajagopal, A., Reddy, K. S. S., & Ramakrishna, B. Plasticity based material model for concrete subjected to dynamic loadings. Int. J. Impact Eng., 2020; 142, 103581.

Declaration of interests

☒ The authors declare that they have no known competing financial interests or personal relationships that could have appeared to influence the work reported in this paper.

☐ The authors declare the following financial interests/personal relationships which may be considered as potential competing interests: